RSC Advances

Crystal structure determination, spectroscopic characterization and biological profile of tailored ionic molecular entity, Sn(IV) iminodiacetic acid-piperazinediium conjugate: In vitro DNA/RNA binding studies, Topo I inhibition activity, cytotoxic and systemic toxicity studies

Journal:	*RSC Advances*
Manuscript ID:	RA-ART-11-2014-013718.R1
Article Type:	Paper
Date Submitted by the Author:	26-Dec-2014
Complete List of Authors:	Arjmand, Farukh; Aligarh Muslim University, Chemistry Yousuf, Imtiyaz; Aligarh Muslim University, Chemistry Zaidi, Yusra; Aligarh Muslim University, Department of Zoology Toupet, loïc; Universit&#65533; de Rennes I, Groupe Mati&#65533;re Condens&#65533;e et Mat&#65533;riaux

Crystal structure determination, spectroscopic characterization and biological profile of tailored ionic molecular entity, Sn(IV) iminodiacetic acid–piperazinediium conjugate: *In vitro* DNA/RNA binding studies, Topo I inhibition activity, cytotoxic and systemic toxicity studies

Farukh Arjmand,*[a] Imtiyaz Yousuf,[a] Yusra Zaidi[b] and Loic Toupet[c]

[a]*Department of Chemistry, Aligarh Muslim University, Aligarh 202002, Uttar Pradesh, India*
[b]*Department of Zoology, Aligarh Muslim University, Aligarh 202002, U.P., India*
[c]*Institut de Physique de Rennes, UMR 625, Université de Rennes 1*, *Campus de Beaulieu Bat. 11 A, 263 av. Général Leclerc*, *35042 Rennes Cedex*, *France*

*E−mail: farukh_arjmand@yahoo.co.in. *Corresponding author. Tel.: +91 5712703893.

Novel ionic tin(IV) iminodiacetic acid−piperazinediium conjugate (**1**) was designed and synthesized as a potential antitumor chemotherapeutic molecular entity and was thoroughly characterized by elemental analysis, FT−IR, ^{1}H, ^{13}C and ^{119}Sn NMR, ESI MS and single crystal X−ray crystallography. Complex **1** resulted from the proton transfer reaction between iminodiacetic acid (H_2IDA) and piperazine (pipz); and its subsequent complexation with tin(IV) chloride salt. **1** crystallized in orthorhombic space group *Ima2* and comprises of an anionic metallic unit, a piperazinediium cation and a chloride ion. In continuity to our previous strategy in search of robust metal−based antitumor drug entities exhibiting reduced systemic toxicity, we have carried out *in vitro* interaction studies of **1** with ct–DNA, tRNA and Topo I targets, to validate its chemotherapeutic potential. Complex **1** exhibited more avid binding propensity with RNA which was reflected by its higher K_b and K values with RNA as compared to DNA. Topoisomerase inhibition activity of **1** was performed by gel electrophoresis which revealed significant inhibitory effect on the catalytic activity of the enzyme at 30 μM concentration. Molecular docking studies of the complex were carried out with DNA (PDB ID: 1BNA), RNA

(PDB ID: 6TNA) and Topo I (PDB ID: ISC7) targets to ascertain the specific binding mode thereby substantiated the spectroscopic results. Cytotoxic studies were carried out on a panel of eight human cancer cell lines; U373MG, PC3, Hop62, HL60, HCT15, SK–OV–3, HeLa and MCF7 by SRB assay which revealed significant regression specifically for HCT15, HOP62, MCF7 and SK–OV–3 human cancer cell lines (GI_{50} value < 10) as compared to the standard drug Adriamycin. Systemic toxicity of **1** was carried out by the estimation of oxidative stress biomarkers such as lipid peroxides (expressed as malondialdehyde; MDA) and reduced glutathione (GSH) levels in kidney and liver homogenates and the study was supported by the histopathologic examination of kidney and liver of female Wistar rats.

Introduction

Cancer– a malignant neoplasm is a complex disease and one of the alarming health concerns of mankind (the global economic toll is 20 percent higher in cancer than other major diseases *viz.*, cardiovascular diseases, cerebrovascular diseases, HIV/AIDS, lower respiratory infection including pneumonia, malaria, and cirrhosis) at $895 billion in 2008. Globally, there is a rise in cancer incidence which is predicted to increase from 12.8 million new cases in 2008 to 22.2 million in 2030.[1,2] The complexity of the disease arises mainly due to the fact that cancers evolve from different tissues of origin, show multiple etiologies or endless combinations of genetic or epigenetic alterations. There is however, a need to readdress either the cancer treatment modalities or to diversify/broaden the chemotherapeutic canvass; the classical approach of treating cancers by chemotherapy employing chemotherapeutic agents *viz*., cisplatin,[3] bleomycin[4] and taxol® (paclitaxel)[5] is noteworthy, nevertheless, the challenges pertaining to clinical inefficiency against resistant tumors and manifestation of systemic toxicity still remain. Plethora of other metal–based compounds have demonstrated significant cytotoxic and

antimetastatic properties with reduced side effects but remained underway in one or other clinical phase.[6,7] Among them are two promising Ru(III) drug candidates, imidazolium [trans–$RuCl_4$(1*H*–imidazole) (DMSO−S)] (NAMI−A) and indazolium [trans–$RuCl_4$(1*H*–indazole)$_2$] (KP1019) which have successfully completed phase I clinical trials and are now undergoing further clinical evaluation. NAMI–A and KP1019 are ionic Ru(III) compounds bearing structural novelty by possessing negatively charged octahedral metal center coordinated to heterocyclic nitrogen donor ligands and equatorial chlorides; a protonated form of the heterocyclic nitrogen ligands as counter ions that are replacable by sodium or other cations.[8–10] The choice of counter ions has been found to influence the solubility and specificity for biomolecule binding of these active compounds. Nevertheless, NAMI–A is active only towards secondary metastasis tumors but inactive towards primary tumors, and is reported to have little cytotoxicity towards many cancer cell lines.[11]

The development of tailored drugs for different cancers is yet at cradle and a very few drugs are entering in preclinical and clinical testing and at a later stage they fail to qualify as drugs, consequently, a lot of setback to pharmaceutical R&D's is obvious. There is a quest for the design of novel cancer chemotherapeutics which are efficacious, robust, and exhibit a different mode of action of cell death at the molecular level. Considerable efforts are being undertaken for developing new drugs/or through optimization of the drug protocols involving combination cocktails of present chemotherapeutic agents with a bioactive organic pharmacophore. A rational drug design is required to achieve specific targeting features and lower systemic toxicity which could arbitrarily be done by choosing appropriate metal ion and tailoring of ligand scaffold etc. Among the emerging class of non–platinum chemotherapeutic is tin(IV) based metal complexes which are established as effective antitumor and antiproliferative agents, their IC_{50} data is

remarkably good (with typical ID_{50} values obtained for these compounds were in the range 50 ng ml^{-1} against MCF−7 and 300 ng ml^{-1} against WiDr).[12] Tin complexes exhibit different mechanism of action at molecular level, a wide spectrum of activity, have potential to overcome platinum–resistance and may possess less or different toxicity as compared to platinum compounds. In tin(IV) derivatives, the metal center acts as a strong Lewis acid which allows the expansion of the coordination number by the addition of ligands or solvent molecule, thereby enhancing the coordination and altering the geometry from the usual trigonal bipyramidal to distorted octahedral. Literature reports reveal that tin(IV) based complexes may bind to glycoproteins or to cellular proteins, and directly interact with DNA, causing cell death by apoptotic mechanism.[13]

We report herein, tailored chemotherapeutic drug entity (**1**) tin(IV) iminodiacetate with piperazinediium as a counter ion. To the best of our knowledge, this is the first demonstration of ionic tin(IV) carboxylate–piperazinediium salt exhibiting remarkably high cytotoxic activity. There are however, scarce examples of ionic tin(IV) complexes which were evaluated for antitumor activity.[14] Previously, some double piperazinediium–M(II){M(II) = Cu(II), Co(II), Zn(II)} sulfates were synthesized as catalysis for organic diastereoselective transformation.[15,16] Since our interest was to find a lead metal–based antitumor drug candidate, we have therefore carried out *in vitro* binding studies of ionic tin(IV) iminodiacetic acid–piperazinediium conjugate (**1**) with multiple targets of drugs *viz*., DNA, RNA and Topoisomerase I. Complex **1** bears structural novelty as a chemotherapeutic molecular entity possessing a dianaionic iminodiacetate trichlorotin(IV) chloride moiety that acts in synergy with the dicationic piperazinediium counter ion to undergo multiple binding interactions at the site of action selectively in cancerous tissues leaving healthy or normal cells unaffected. Most of the chemotherapeutic drugs targeting DNA

primarily exert their anticancer activity by altering DNA replication, thereby inhibiting growth of tumor cells. More recently RNA's particularly microRNAs (miRNAs) have emerged as therapeutic targets for cancer therapy since the abnormal expression of these noncoding RNAs is associated with the pathogenesis of human cancer.[17] The specific recognition of pockets available in RNA by suitable ligands involving non–covalent binding usually based on van der Waals forces, electrostatic interactions and surface complementarity is considered to be an important asset for RNA targeted therapeutics.[18] DNA topoisomerases are highly expressed in most of the cancerous cells (kidney, colon, prostate, ovary and esophagus); by inhibiting the topoisomerase enzyme activity, a drug entity can result in a cell cycle arrest and cause apoptosis. Minor groove analogs such as camptothecin, Hoechst 33258 and their derivatives have empirically validated Topo I as an anticancer drug target.[19,20]

The cytotoxic activity of **1** was validated against a panel of different human cancer cell lines (U373MG, PC3, Hop62, HL60, HCT15, SK–OV–3, HeLa and MCF7) employing SRB assay. Systemic toxicity of **1** was carried out by the estimation of oxidative stress biomarkers (lipid peroxides and GSH levels) and histopathology of kidney and liver tissues of female Wistar rats which revealed that **1** did not manifest toxicity at dose of 2.4 mg kg^{-1} as compared to control leaving the normal tissues unaffected.

Results and discussion

Synthesis and structural characterization

Complex **1** was synthesized by reacting methanolic solutions of iminodiacetic acid (H_2IDA), piperazine and $SnCl_4.5H_2O$ in 1:1:1 stiochiometric ratio as depicted in Scheme **1**. Complex **1** resulted from *insitu* proton transfer reaction resulting in ion pair, $\{(pipz)^{+2}(IDA)^{-2}\}$ between iminodiacetic acid (H_2IDA) and piperazine (pipz); and its subsequent reaction with tin(IV)

chloride (Fig. 1). The synthesized complex was stable towards air and was found soluble in organic solvents like $CHCl_3$, DMF and DMSO. The molecular structure of **1** was established by X–ray diffraction studies which was further corroborated by elemental analysis and other spectroscopic measurements (UV−vis, FT–IR, NMR and ESI–MS).

Complex **1** crystallized in orthorhombic space group *Ima2* and comprises of an anionic metallic unit, one piperazinediium cation and a chloride ion. The asymmetric anionic unit, $[SnCl_3(IDA)]^{2-}$ consists of one Sn(IV) atom coordinated to one iminodiacetate ligand moiety (IDA^{2-}) and three chlorine atoms. Sn(IV) atom is located on a symmetry center and has the overall geometry of a slightly tetragonally distorted octahedron. The equatorial coordination basal plane is formed by two O atoms (O1) of IDA^{2-} and two chlorine atoms (Cl1) while the axial positions were occupied by one chlorine atom (Cl2) and a N atom (N1) of IDA^{2-} moiety (Fig. 2a). Therefore, a coordination environment of $SnNO_2Cl_3$ unit is formed having Sn1–O1 = 2.0894(19) A°, Sn1–N1 = 2.222(3) A°, Sn1–Cl1= 2.3670(8) A° and Sn1–Cl1= 2.3510(10) A°. A smaller bite angle, O(1)–Sn(1)–N(1) of 78.32° is primarily responsible for distortion from the regular octahedral geometry. Selected bond lengths and bond angles are listed in Table S1. All the Sn–O, Sn–N and Sn–N bond distances have been found within the range reported for octahedral Sn(IV) complexes.[21] Positively charged piperazinediium cationic species adopts a usual chair form conformation at the equatorial site. The crystal structure is mainly stabilized by a network of O—H···O and N—H···O hydrogen bonding interactions between H2A of piperazinediium cation and O atom (O1) of IDA^{2-} group of the anionic metal center (H2A·····O1= 2.004 A°). Additionally, N atom (N1) of IDA^{2-} was actively engaged in the H−bonding interactions with the Cl (Cl3) atom of the crystal lattice (Cl3·····O1= 2.222 A°, Fig. 2b). The molecules are packed along the basis involving $[NH_2]^+$/Cl3 interactions that reinforce crystal

structure cohesion and lead to the formation of stabilized supramolecular framework in the crystal lattice (Fig. S1).

In the IR spectrum of complex **1**, a broad characterictic band in the range 3400–3250 cm^{-1} corresponding to O–H stretching frequency of COOH group of H_2IDA moiety was found absent which confirmed its coordination to metal *via* deprotonation. Two IR frequency bands corresponding to *ν*(N–H) and ν(CH_2) group vibrations were observed at 3127 and 2922 cm^{-1}, respectively. The characteristic peaks of ν_{asym}(C=O) and ν_{sym}(C=O) stretching vibrations were displayed at 1670 and 1453 cm^{-1}, respectively with $\Delta=[\nu_{asym}(C=O)-\nu_{sym}(C=O)]$ 217 cm^{-1} value, indicative of monodentate coordination mode for the iminodiacetic acid. Additionally, the formation of **1** was also ascertained by the presence of medium intensity bands at 525, 446 and 357 cm^{-1} corresponding to Sn–O, Sn–N and Sn−Cl vibrations, respectively.[22]

^{1}H NMR spectrum of **1** did not display O–H proton signal of the H_2IDA expected in range of 10–13 ppm, confirming its deprotonation. A sharp signal at 4.03 ppm and a singlet at 3.79 ppm were attributed to $[NH_2]^+$ protons and CH_2 protons of the piprazinediium moiety $(pipzH_2)^{+2}$, respectively.[23] Moreover, a multiplet and a singlet corresponding to −NH and $-CH_2$ protons of IDA^{2-} group were found at 3.75 and 3.36 ppm, respectively. The ^{13}C NMR spectrum of the complex **1** displayed a prominent resonance peak at 162 ppm assigned to carboxylate carbons of IDA^{2-}. Two resonance signatures of CH_2 carbons of piperazinediium and IDA^{2-} moieties were found in the range 67.96−57.91 ppm.

^{119}Sn NMR spectrum exhibited a strong signal at −499.74 ppm consistent with the octahedral geometry around the Sn(IV) ion (Fig. S2).[24]

The ESI–MS spectra (Figure S3) of **1** revealed molecular ion peak at *m/z* 479 for $[C_8H_{17}N_3O_4Cl_4Sn]^+$. Fragmentation peaks at *m/z* 447 and 411 corresponding to

$[C_8H_{17}N_3O_4Cl_4Sn–Cl+3H]^+$ and $[C_8H_{17}N_3O_4Cl_4Sn–2Cl+3H]^+$ fragments, respectively were also observed.

***In vitro* DNA/RNA binding studies**

DNA is primary target for most of the antitumor chemotherapeutic agents as it offers a variety of potential metal−binding sites. Such sites are either electron rich nucleobases or phosphate oxygen atoms of the DNA duplex. Metal complexes usually bind to nucleic acids *via* covalent or non–covalent binding modes (electrostatic, groove binding and intercalation). Electrostatic binding mode contributes considerably to binding affinities in charged molecules, which predominantly recognize nucleic acids. On the other hand, RNA exhibits a high diversity in terms of folding and conformations, therefore, has a greater potential for selective targeting based on structure rather than sequence. This structural feature allows it to interact *via* non–covalent interactions *viz.,* electrostatic, hydrogen bonding, van der Waals interaction, etc. with the drug entities.

Electronic absorption spectroscopy is one of the most useful techniques to examine the metal complex−DNA/RNA interactions. UV–vis spectrum of **1** exhibited an intense absorption band centered at 270 nm attributable to $n\rightarrow\pi^*$ transition of iminodiacetic acid moiety. On addition of aliquots of ct−DNA/tRNA (0.00–6.00 x 10^{-5} M) to a fixed concentration of complex **1** (1.66 x 10^{-4} M), a significant 'hyperchromism' of 37% and 43% was observed for ct–DNA and yeast tRNA, respectively with a blue shift of 2−4 nm which implicated strong binding affinity of **1** involving electrostatic interaction mode *via* external contact (Fig. 3a and b). The 'hyperchromic effect' along with a blue shift is typical of cationic complexes that involve non–covalent interactions preferably external contact (surface binding) *via* electrostatic binding to outside of DNA/RNA helix. Hyperchromism is usually associated with the breakage of the hydrogen bonds

that stabilize the secondary structure of nucleic acids.[25] The stronger affinity of **1** could also be substantiated by the presence of hard Lewis acidic Sn(IV) ion which preferably binds to a negatively charged phosphate group of the DNA/RNA backbone causing contraction and conformational change in the helix.[26] In addition, the hydrogen–bonding interactions involving –NH/–COO^- groups of IDA or $(–NH_2)^+$ groups of piperazinediium with DAT groups positioned on the edge of the DNA/RNA nucleobases contribute to the stability of complex **1**–DNA/RNA adduct.[27]

In order to further elucidate the quantitative binding strength of **1** with ct–DNA and yeast tRNA, intrinsic binding constant, K_b values of the complex were determined by monitoring changes in absorbance with increasing concentration of ct–DNA and yeast tRNA given by Eq. (**1**)

$$\frac{[\text{DNA or RNA}]}{(\varepsilon_a - \varepsilon_f)} = \frac{[\text{DNA or RNA}]}{(\varepsilon_b - \varepsilon_f)} + \frac{1}{K_b(\varepsilon_b - \varepsilon_f)} \qquad \textbf{(1)}$$

where [DNA or RNA] are the DNA or RNA concentration, and ε_a, ε_f and ε_b are the apparent (A_{abs}/[complex **1**]), free and bound complex extinction coefficients, respectively. In a plot of [DNA or RNA]/(ε_a–ε_f) *vs*. [DNA or RNA] with a slope of 1/(ε_b–ε_f) and intercept of 1/[K_b(ε_b–ε_f)], K_b values were obtained by the ratio of the slope to the intercept. The intrinsic binding constant values K_b for the complex with ct–DNA or yeast tRNA is being presented in Table **1**.

The binding constant values, K_b demonstrated stronger binding propensity of **1** towards yeast tRNA as compared to ct–DNA for which a plausible explanation could be that the yeast tRNA exhibits A–form conformations with L–shaped tertiary structure possessing wide shallow minor groove and a pulled–in narrow major grooves. This structural feature allows its base pairs to remain well exposed and easily accessible for the drug entities. Moreover, **1** could exhibit higher

affinity towards the bulge region of yeast tRNA, thereby providing a rationale for its stronger binding affinity.[28]

Further insight on interaction mode of complex **1** with nucleic acids was substantiated by the fluorescence studies. In the absence of ct−DNA and tRNA, **1** emitted weak fluorescence in Tris−HCl buffer at ambient temperature with a maxima appearing at *ca*. 390 nm (λ_{ex} = 285 nm). The concomitant addition of ct–DNA/yeast tRNA (0.00–4.00 x 10^{-5} M) to a fixed concentration of complex **1** (1.67 x 10^{-5} M), resulted a significant enhancement in the fluorescence emission intensity with no apparent shift in the shape and position of the emission bands (Fig. S4a and b). The observed enhancement in emission spectra upon binding of the complex **1** with ct−DNA or yeast tRNA is largely due to the changes in the environment of the metal complex from polar to non–polar and is related to the extent to which a complex penetrates inside the hydrophobic environment of the nucleic acids. Moreover, the Sn(IV) metallic core of the complex **1** exhibits a strong electrostatic attraction to the anionic phosphate backbone of DNA, thus precluding substantial overlap with the base pairs that leads to the higher emission intensity. The binding constants, *K* values as quantified by Scatchard equation[29] were found to be 4.13 x 10^4 and 5.86 x 10^4 M^{-1} for ct−DNA and yeast tRNA, respectively.

CD titration experiments were performed as a function of complex concentration to monitor the conformational changes in DNA/RNA and the binding mode of **1** upon interaction with the nucleic acids. The CD spectrum of DNA exhibited a positive band at 275 nm due to base stacking and a negative band at 245 nm due to the right–handed helicity, which are quite sensitive to the mode of DNA interactions with small molecules. Simple groove binding and electrostatic interaction of the complexes could lead to slight perturbation of the intrinsic CD profile of DNA; On the other hand an intercalating molecule enhances the intensities of both

bands due to disruption of the stacking of the nucleobases on intercalation.[30] Upon addition of complex **1** to ct–DNA, ([complex **1**]/[DNA] = 1), the CD spectrum undergoes decrease in intensity in both the positive (helicity) and negative (ellipticity) bands without any significant shifts as illustrated in Fig. S5a. The decrease in the intensity of positive and negative bands by **1** could be due to unwinding of DNA helix that leads to the loss in DNA helicity thereby validating the electrostatic binding mode of **1** towards DNA.[31]

The CD spectrum of tRNA depicted characteristic four major peaks at 207 and 240 nm (negative), 225 and 270 nm (positive) consistent with A–conformation of tRNA. Upon addition of complex **1** to tRNA solution (r = [complex **1**]/[tRNA] = 1) a significant amplification of a negative band along with a prominent blue shift at 207 nm (ellipticity band) was observed while positive bands at 225 and 270 nm (base stacking) showed relatively less decrease in intensities with no shift in the bands (Fig. S5b). The reduction in intensity of the band at 270 nm, in the spectra of complex **1**–tRNA system along with the major intensity changes of the bands at 210 and 227 nm could be due to the aggregate formation of tRNA upon complexation.[32,33]

Besides X–ray crystallography and high resolution NMR, hydrodynamic studies such as viscometric measurements serve as an unambiguous tool to determine the binding mode of small molecules towards DNA. Classical intercalators like EB tend to increase the length of the DNA helix, due to the accommodation of the ligand in between the base pairs of ct−DNA resulting in an increase in the DNA viscosity. However, complexes that bind either electrostatically *via* sugar−phosphate backbone produce bends or kinks in the DNA helix reducing its effective length and its viscosity, while DNA groove binding under the identical experimental conditions essentially results in little or no effect on DNA viscosity.[34] Plots of relative viscosity, $(\eta/\eta_o)^{1/3}$ *vs.* [Compound]/[DNA] shown in Fig. S6 demonstrated a decrease in DNA viscosity with increase

in [Compound]/[DNA] ratio, thereby implying that **1** binds ct–DNA strongly by simple electrostatic mode *via* sugar–phosphate backbone. In contrast, no obvious change in relative viscosity was observed for yeast tRNA upon addition of complex **1** owing to its non–linear L–shaped tertiary structure.[35]

IR spectroscopy was used to study the complex **1**–DNA/RNA interactions in the mid IR (1800−800 cm^{-1}) frequency bands. Significant spectral perturbations in the shape and position of vibration band(s) corresponding to the different nitrogenous bases and the phosphate backbone vibration frequencies of ct–DNA were observed upon the addition of complex **1**. As depicted in Figure S7a, a prominent shift of the guanine band at 1710 cm^{-1} (guanine–C=O stretch) to a lower frequency at 1690 cm^{-1} for **1**–DNA complex was observed. No major alteration in the thymine band (thymine−O2) at 1680 was noticed. Similarly, the adenine band at 1615 cm^{-1} (adenine–N7) exhibited a slight shift without any change in absorption intensity due to weak metal complex–adenine interaction. However, important shift and intensity variation was observed for cytosine band at 1491 cm^{-1}, attributed to strong metal complex–cytosine binding interactions. Furthermore, DNA is characterized by the spectral alterations of the PO_2 asymmetric and symmetric bands at *ca*. 1225 and 1090 cm^{-1}, respectively which were shifted towards lower frequencies at 1210 and 1070 cm^{-1}, respectively. The observed spectral shift was also accompanied by the prominent intensity variations of the phosphate bands. The observed spectral changes could be attributed to the complex–phosphate interaction, and the presence of hard Lewis acid, Sn(IV) atom which specifically binds to phosphate backbone of DNA and thus contributes to the stabilization of metal complex–DNA interaction.[36,37]

In case of yeast tRNA, in plane vibration band corresponding to guanine bands at 1720 cm^{-1} was shifted to 1705 cm^{-1} in tRNA–**1** complex. Similarly, the band at 1650 cm^{-1} (mainly uracil)

shifted towards a higher frequency at 1655 cm^{-1}, but the band at 1615 cm^{-1} (mainly adenine) exhibited major upward shifting to 1630 cm^{-1} upon complex **1**–tRNA complexation (Figure S7b). PO_2 asymmetric bands at 1225 cm^{-1} revealed a remarkable shift and intensity variations to 1240 cm^{-1} attributed to strong complex **1** phosphate backbone interaction. The spectral perturbations observed for guanine, uracil, and adenine bands are indicative of interaction of complex **1** with guanine and uracil reactive sites and as well as to the phosphate backbone of RNA . However, there was no major shift or intensity change in the marker IR frequency bands corresponding to the ribose–phosphate vibrations at 862 and 810 cm^{-1}, thus it can proposed that tRNA is in the A–conformational structure.[38,39]

DNA cleavage studies

The DNA cleavage activity for complex **1** was analyzed by monitoring the conversion of supercoiled DNA (Form I) into nicked form (Form II) or linear form (Form III). Briefly, a concentration–dependent experiment was performed to ascertain the ability of complex **1** to cleave SC DNA in the absence of any reducing agent. Upon increasing the concentration of metal complex from 10–50 μM (Fig. 4, Lane 2–6) the effect on DNA mobility was negligible and even at higher concentration (50 μM) there was a little conversion of the plasmid DNA from Form I (SC) to Form II (NC) (Lanes 3–5). Literature reports reveal that small molecules which are capable of showing electrostatic interaction with DNA do not influence the mobility of supercoiled form of plasmid DNA. Our results implicated that ionic tin(IV) complex **1** could not exhibit the discernible cleavage pathway, however, the cytotoxicity against tested human cancer cell lines can be attributed to the high affinity of complex towards DNA. In addition, interaction of **1** with DNA can thus be interpreted *via* electrostatic interaction by the involvement of external phosphate groups.[40,41] Moreover, interaction of tin(IV) based compounds with DNA is not

sequence–base–specific as may be expected for cleavage–mediated cell death mechanism witnessed by most of the transitional metal–based complexes.

Topoisomerase I inhibitory assay

Topoisomerase enzymes (type I and II) are essential for cellular events *viz*., DNA replication, recombination, chromosome segregation and gene transcription. Topo I relaxes DNA by transiently breaking and religating one strand of duplex DNA (in contrast to Topo II which relaxes both strands of duplex).[42] The catalytic mechanism is initiated by a nucleophilic attack of active site tyrosine –OH group on the phosphate group at 3′–end of the broken strand which results in the breaking of the DNA phosphodiester bond and the formation of a binary DNA–Topo I covalent complex (cleavable complex). These reactions are highly reversible and the religation process occurs faster than cleavage so the equilibrium favors the uncleaved DNA. (Scheme 2). However, the rate of religation is inhibited or reduced in presence of Topo I inhibitors, like camptothecin that results in apoptotical death of cancer cells.[43,44]

A standard cleavage assay was employed to investigate the effects of **1** on human Topo I by gel electrophoresis as depicted in the Fig. 5. This assay provides a direct means of determining whether the drug affects the unwinding of a supercoiled (SC) duplex DNA to nicked open circular (NOC) and relaxed (R) DNA The disappearance of SC DNA (fastest band) and the appearance of bands for NOC DNA (slowest band) and R DNA (which migrates between SC and NOC band) will be observed if Topo I catalytic activity is intact. On the contrary, if the activity of the enzyme was inhibited, no R or NOC DNA would be detected. When catalytic activity of topoisomerase **1** was assayed, complex **1** inhibited this process in a concentration–dependent manner. It was observed that supercoiled DNA was fully relaxed with the topoisomerase I enzyme in the absence of **1** (Lane 2, Fig. 5). However, upon increasing the concentration of

complex **1** the levels of relaxed form were inhibited (Lanes 3–6) and at a concentration of 30 μM (Lane 6) total inhibition of relaxed form was observed.

Molecular docking studies

Molecular docking studies provide important implications for the rational design and synthesis of robust drug entities that selectively target and recognize the preferred binding sites of nucleic acids and proteins. These studies offer the visual representation of the binding of small ligands to DNA, thereby provide concrete evidence and substantiate the spectroscopic results. The resulting docking experiments revealed that **1** interacts with B–DNA (PDB ID: 1BNA) adjacent to the GC−rich sequence of the minor groove. The minor groove is in particular an attractive target for small molecules being inherently flexible and the closer proximity of the strands in the minor groove allows more contact surface area for a small molecule to bind tightly.[45] Recognition of the DNA minor groove by complex **1** could be attributed to the appropriate match in shape between the complex and the GC region (G2, C3, G4, G21, G22 and G23) allowing it to fit into the groove with little steric hindrance.[46] Additional stabilization could be offered by hydrogen bonding interactions between the carbonyl O atoms (O1 and O2) of iminodiacetate group and H–atoms of G4 and G22 minor groove base pairs (Fig. 6).

Complex **1** was also successively docked towards the molecular target, yeast tRNA (PDB ID: 6TNA) in order to determine the preferred binding sites on tRNA. Yeast tRNA has well defined 3D structures including regions like D arm, acceptor stem, T arm, ψ loop and anticodon arm shown in Fig. 7. These structural motifs participate directly or indirectly with the targets for specific base pair recognition process. The resulting docked model depicted in Fig. 8 implied that **1** was inserted into the active pocket of the anticodon arm in close proximity of C−40, A−35, A−36, A−38, G−30, C−40, U−41, C−28 and A−29.[47] This structural feature of **1** allows it to

form multiple intermolecular H–bonds, considered on the basis of 3A˚ distance between the Cl atoms (H–bonding donor groups) and O2 atom of A36 and A29. In addition to these forces, van der Waals contributions and hydrophobic interactions play a major role in the stronger binding of complex **1** to yeast tRNA.

The resulting binding energies calculated for the best docked pose of **1** with the ct–DNA and yeast tRNA targets were found to be –237 and –267 KJ mol^{-1}, respectively. More negative binding energy value signify greater binding propensity of a metal complex, which correlates well with our *in vitro* DNA and RNA binding experiments. Thus, a mutual complement existed between spectroscopic techniques and the molecular docking studies

In order to validate the Topo I inhibitory activity of complex **1** and to search the exact binding site of action, docking studies of **1** were carried out with the target active–site of human–DNA–Topo I complex (PDB ID: 1SC7). Human–DNA–Topo I complex (PDB ID: 1SC7) was retrieved from Protein Data Bank in which Topo I is bound to the oligonucleotide sequence 5′–AAAAAGACTTsX–GAAAATTTTT–3′, where 's' is 5′–bridging phosphorothiolate of the cleaved strand and 'X' represents any of the four bases A, G, C or T. The phosphodiester bond of G12 in 1SC7 was rebuilt and SH of G11 on the scissile strand was changed to OH.[48] The speculations regarding the detailed binding pattern of complex **1** with Topo I were made for the best docked conformation which revealed that **1** approached towards the DNA cleavage site in the enzyme and formed a stable complex involving significant interactions between the purine of G12 (+1) and pyrimidine ring of T10 (–1) in the minor groove of the scissile strand; and at C117 and A114 on the non–scissile strand, parallel to the plane of base pairs (Fig. 9a). The insertion of the complex between the DNA base pairs at the cleavage site resulted an increase in the physical distance between the cleaved DNA termini and

consequently inhibition of the religation step was catalyzed by Topo I.[49] Moreover, carbonyl O atom of iminodiacetate moiety acts as a hydrogen bond acceptor and forms H–bond with Asn 352 and Lys 354 residues, which are important amino acids that interact with the drug entities in the DNA–Topo I active site, subsequently leading to inhibitory effect on Topo I. Furthermore, other hydrogen bonding interactions between the protonated NH_2^+ group of piperazinediium moiety and cyt 112 residues also contribute to the extra stability of **1**–Topo I complex (Fig. 9b). The resulting calculated binding energy of Topo I docked complex **1** was found to be –237 KJ mol^{-1}.

***In vitro* cytotoxic activity**

The *in vitro* cytotoxic activity of complex **1** was evaluated in terms of GI_{50} (concentration of drug that produces 50% inhibition of the cells), TGI (concentration of the drug that produces total inhibition of the cells) and LC_{50} (concentration of the drug that kills 50% of the cells) values by semi–automated Sulforhodamine–B (SRB) assay,[50] against a panel of eight human carcinoma cell lines of different histological origin, *viz.*, U373MG (CNS), PC3 (prostrate), Hop62 (lung), HL60 (leukemia), HCT15 (colon), SK–OV–3 (ovarian), HeLa (cervix) and MCF7 (human breast) (Table 2). These results revealed a pronounced GI_{50} values < 10 μg/mL towards all tested cancer cell lines except U373MG (CNS) cell line. The antitumor screening data depicted in Fig. 10, shows % control growth *vs.* drug concentration (μgml^{-1}) against different human carcinoma cell lines which provide authentic evidence in favor of **1** as antitumor drug entity.

***In vivo* systemic toxicity studies**

Effect of complex 1 on oxidative stress markers. It is well known that the high levels of free radicals and reactive oxygen species (ROS) cause oxidative damage to cell which contributes

substantially to lipids and protein damage in liver and kidney of rats. Thus, to determine oxidative stress induced by **1** after 24 h treatments in liver and kidney tissues of rats, the levels of reduced glutathione (GSH) and malondialdehyde (MDA) were measured at single doses of 2.4 and 4.8 mg/kg and the results are shown in Table 3 and 4, respectively. In liver and kidney, a dosage of 4.8 mg/kg of **1** caused significant decrease in the levels of reduced GSH and increase in MDA levels, whereas these changes were found to be insignificant at 2.4 mg/kg dose of **1**, as compared to control ($p = 0.05$), respectively. However, the decrease in level of reduced GSH and increase of MDA levels were higher in kidney as compared to liver of drug–treated rats. Altogether, these results indicate that the chemical entity **1** at dose of 4.8 mg/kg causes overproduction of ROS as evident from depletion of reduced GSH and increased MDA levels whereas, no significant ROS were produced after a treatment of 2.4 mg/kg in liver and kidney of complex **1**–treated rats. However, cisplatin (CDDP), at equivalent doses, showed overproduction of ROS (ref) leading to significant systemic toxicity in kidney and liver tissues of rats. [51]

Histopathologic examination of liver and kidney tissues. Light microscopic observation revealed that the control kidney tissue showed normal histology of glomeruli, distal and proximal tubules. In contrast, the kidney of rats treated with complex **1** at a dose of 4.8 mg/kg was characterized by marked lymphocytic infiltrate in glomeruli and pyknotic nuclei, as depicted in Fig. 11(A–C), whereas no such alterations were found at a dose of 2.4 mg/kg of **1**.

Furthermore, in case of liver tissues, control showed normal large polygonal cells with prominent nuclei with eosinophilic cytoplasm and few spaced sinusoids arrangement. In contrast, the group receiving complex **1** ip at a single dose of 4.8 mg/kg showed hepatotoxicity, particularly degeneration of hepatic cords, inflammation, and congestion of portal vein whereas,

no significant histopathologic alterations in liver of rats treated at a dose of 2.4 mg/kg of **1** were observed (Fig. 11(D–F).

Conclusions

Novel ionic tin(IV) iminodiacetic acid–piperazinediium conjugate (**1**) was synthesized and characterized by various spectroscopic techniques (FT–IR, ^{1}H, ^{13}C and ^{119}Sn NMR, ESI−MS) and single X–ray diffraction crystallography. **1** crystallized in orthorhombic space group, *Ima2* and comprises of an anionic metallic unit, a piperazinediium cation and a chloride ion. *In vitro* interaction studies of **1** with ct−DNA, tRNA and Topo I targets was carried out to validate its chemotherapeutic potential. The results revealed that complex **1** interacts with ct−DNA and yeast tRNA *via* electrostatic mode of binding preferably through oxygen atoms of the sugar phosphate helix of DNA/RNA. Interestingly, **1** exhibited more avid binding propensity towards RNA, which was substantiated by the larger K_b and K values of **1** with RNA as compared to DNA. A concentration dependent cleavage activity of **1** on pBR322 DNA revealed no significant inhibition even at high concentration thereby revealing electrostatic mode of binding. Complex **1** exhibited significant inhibitory effects on Topo I enzymatic activity at 30 μM. *In vitro* cytotoxicity on a panel of human cancer cell lines revealed significant regression in HCT15, HOP62, MCF7 and SK−OV−3 cancerous cells as compared to the standard drug with GI_{50} value < 10. High cytotoxicity of **1** towards human cancer cells was accompanied by manageable systemic toxicity as was evident from the insignificant changes in GSH and MDA levels with no alterations in histology of liver and kidney in healthy female Wistar rats. Complex **1** is indeed a potent cytotoxic agent and higher doses of **1** can be administered safely, thus opening a wider therapeutic window which warrants further *in vivo* anticancer investigation.

Experimental section

Materials and instrumentation. Commercially obtained chemicals were used as received without further purification. Iminodiacetic acid (Alfa Aesar), $SnCl_4.5H_2O$, tris–(hydroxymethyl)aminomethane (tris–buffer) (Merck). Calf thymus DNA (ct–DNA) and yeast tRNA (Type IX from Torula yeast) were purchased from Sigma Co. and were stored at 4 $^{\circ}$C, 6X loading dye (Fermental Life Science) and Supercoiled plasmid DNA pBR322 (Genei), and Human–Topoisomerase–I enzyme (CalBioChem).

Elemental analysis was carried out on Carlo Erba Analyser Model 1106. Molar conductance was measured at room temperature on Eutech con 510 electronic conductivity bridge. Fourier–transform infrared (FT–IR) spectra were recorded on an Interspec 2020 and Spectrum Two (Pelkin Elmer) FT–IR spectrometers. ESI–MS spectra were recorded on Micromass Quattro II triple quadrupole mass spectrometer. NMR (^{1}H, ^{13}C and ^{119}Sn) spectra were obtained on a Bruker DRX–400 spectrometer with Me_2SO–d_6 as solvent. Electronic spectra were recorded on UV–1700 PharmaSpec UV–vis spectrophotometer (Shimadzu) in DMSO using cuvettes of 1 cm path length and data were reported in λ_{max}/nm. Emission spectra were made on Shimadzu RF–5301PC Spectrofluorophotometer. All the experiments involving the interaction of the complex with ct–DNA and the yeast tRNA were carried out in aerated buffer (5mM Tris–HCl, 50mM NaCl, pH = 7.2). The concentration per base pairs for both DNA and RNA was determined spectrophotometrically by assuming ε_{260nm} values to be 6600 and 7700 $M^{-1}cm^{-1}$ respectively.[52,53] The viscosity measurements were carried out using Oswald capillary viscometer maintained at 25 °C. CD spectra were measured on Jasco J–815–CD spectropolarimeter at room temperature. Cleavage experiments were performed with the help of Axygen electrophoresis supported by a Genei power supply with a potential range of 50–500 V, visualized and photographed by Vilber–INFINITY gel documentation system.

Synthesis of ($pipzH_2$)[Sn(IDA)Cl_3)].Cl (1). To a methanolic solution of Iminodiacetic acid (H_2IDA) (0.399 g, 3 mmol), piperazine (pipz) (0.258 g, 3 mmol) was added drop wise, followed by the addition of a methanolic solution of $SnCl_4$. $5H_2O$ (1.05 g, 3 mmol) and the reaction mixture was kept on a reflux. A white precipitate formed after 6 h of stirring and reflux was filtered, washed with hexane and dried *in vacuo.* Suitable crystals for single X–ray crystallography analysis were obtained after recrystallization from the mixture of DMSO–MeOH in a ratio of 8:2.

Yield: 70%, M.p. 260 °C. Anal. Calcd. for $C_8H_{17}N_3O_4Cl_4Sn$ (%): C, 20.05; H, 3.58; N, 8.77: Found C, 20.18; H, 3.66; N, 8.67. IR (KBr, ν_{max}/cm^{-1}): 3127 ν(N–H); 2922 ν(–CH_2); 1670 ν_{asym}(C=O); 1453 ν_{sym}(C=O); 525 ν(Sn–O), 446 ν(Sn–N); 357 ν(Sn−Cl). ^{1}H NMR (400 MHz, DMSO−d6, ppm): 4.03 (br, 4H, NH_2, pipzH_2^{2+}), 3.79 (s, 8H, CH_2, pipzH_2^{2+}), 3.75 (q, 1H, N*H,* IDA), 3.36 (s, 4H, CH_2–C=O, IDA). ^{13}C NMR (100 MHz, DMSO−d6, ppm): 162 (–*C*=O), 62.96 (–*C*H_2, pipz), 57.91 (–*C*H_2–NH–). ^{119}Sn NMR (149.19 MHz, DMSO−d_6, ppm): −499.74, ESI–MS (*m/z*): 479.9 $[C_8H_{17}N_3O_4Cl_4Sn]^+$.

Description of X–ray crystal structure. Suitable X–ray quality crystals of the complex **1** were obtained after slow evaporation of the reaction mixture at room temperature. Single crystal X–ray structural studies of complex was performed on a CCD Oxford Diffraction Xcalibur Saphir 3 diffractometer employing graphite–monochromated Mo–Kα radiation generated from a fine–focus sealed tube (λ=0.71073Å) at 140(2) K. Data collection strategy was evaluated by using the CrysAlisPro CCD software. Collections of data were observed by the standard ω scan techniques and were scaled and reduced using CrysAlisPro RED software. The structure was solved by direct methods using SIR–97[54] and refined by least–squares methods on F^2 using SHELXL–97.[55] The positions of all atoms were obtained by direct methods. Anisotropic thermal parameter were

assigned to all non–hydrogen atoms and the remaining hydrogen atoms were placed in geometrically constrained position and refined as riding atoms with a common fixed isotropic thermal parameter. The drawing of the complex was realized with PLATON.[56] A summary of the selected crystallographic information is given in Table 5.

***In vitro* DNA/RNA binding and cleavage experiments.** DNA/RNA binding experiments include absorption spectral traces, emission spectroscopy, viscosity measurements and CD conformed to the standard methods and practices previously adopted by our laboratory.[57–60] While measuring the absorption spectra an equal amount of DNA/RNA was added to both the compound solution and the reference solution to eliminate the absorbance of the ct–DNA/tRNA itself, and Tris buffer was subtracted through base line correction. The cleavage experiments of supercoiled pBR322 DNA (300 ng) by **1** in Tris–HCl/NaCl (5:50 mM) buffer at pH 7.2 was carried out using agarose gel electrophoresis. The samples were incubated for 45 min at 25°C and cleavage process was monitored using agarose gel electrophoresis in a concentration dependent manner. A loading buffer containing 25% bromophenol blue, 0.25% xylene cyanol, 30% glycerol was added and electrophoresis was carried out at 50 V for 1h in Tris–HCl buffer using 1% agarose gel containing 1.0 mg/ml ethidium bromide.

Topoisomerase I inhibition assay. One unit of the enzyme was defined as completely relaxed 1 μg of negatively supercoiled pBR322 DNA in 30 min at 310 K under the standard assay conditions. The reaction mixture (30 μL) contained 35 mM Tris–HCl (pH 8.0), 72 mM KCl, 5 mM $MgCl_2$, 5 mM DTT, 2 mM spermidine, 0.1 mg mL^{-1} BSA, 0.25 μg pBR322 DNA, 2 Unit Topo–I and complex **1**. These reaction mixtures were incubated at 310 K for 30 min, and the reaction was terminated by addition of 4 μL of 5X buffer solution consisting of 0.25%

bromophenol blue, 4.5% SDS and 45% glycerol. The samples were electrophoresed through 1% agarose in TAE at 30 V for 8 h.

Molecular docking studies. Molecular docking studies were performed by using HEX 8.0 software,[61] which is an interactive molecular graphics program for calculating and displaying feasible docking modes of an enzymes and DNA molecule. Structure of the complex **1** was converted it into PDB format from mol format by OPENBABEL (http://www.vcclab.org/lab/babel/). The crystal structure of the B–DNA dodecamer d(CGCGAATTCGCG)$_2$ (PDB ID: 1BNA), RNA (PDB ID: 6TNA) and human–DNA–Topo I (PDB ID: 1SC7) were downloaded from the protein data bank (http://www.rcsb.org./pdb). Visualization of the docked pose has been done by using CHIMERA (www.cgl.ucsf.edu/chimera), PyMol (http://pymol.sourceforge.net/) and Discovery Studio molecular graphics program.

***In vitro* cytotoxic studies.** The *in vitro* antitumor screening of **1** was carried out on following eight human cancer lines of different histological origin *viz.*, A2780 (ovary), Hop62 (lung), U373MG (CNS), PC3 (prostrate), MCF7 (breast), HL60 (leukemia), HeLa (Cervix) and HCT15 (colon). Human malignant cell lines were procured and grown in RPMI–1640 medium supplemented with 10% Fetal Bovine Serum (FBS) and antibiotics to study growth pattern of these cells. The proliferation of the cells upon treatment with chemotherapy was determined by means of the Sulphorhodamine–B (SRB) semi–automated assay. All cell lines were seeded into 96 well plates and cells were counted and cell count was adjusted according to the titration readings so as to give optical density in the linear range (0.5 to 1.8) and were incubated at 37 ºC in CO_2 incubator for 24 h. The stock solution of the complexes were prepared as 100 mg/ml in DMSO and four dilutions i.e. 10 µg/ml, 20 µg/ml, 40 µg/ml, 80 µg/ml, in triplicates were tested,

each well receiving 90µL of cell suspension. The plates were labeled properly and were incubated for 48 h. Termination of experiment was done by gently layering the cells with 50 µL of chilled 30% TCA (in case of adherent cells) and 50% TCA (in case of suspension cell lines) for cell fixation and kept at 4 ºC for 1h. Plates stained with 50 µL of 0.4% SRB for 20 min. All experiments were made in triplicate Table S2.

***In vivo* biochemical studies**

Animals and treatment groups. All *in vivo* experiments were performed on adult female Wistar rats (obtained from the animal house of JNMC, Aligarh Muslim University, Aligarh) weighing 150 ± 50 g. The rats were kept under standard laboratory conditions (23 ± 2ºC, 12 h light/dark cycle) and had access to standard rat chow and clean drinking water provided *ad libitum*. All the animals were let in their cages for at least 2−3 days before the beginning of the experiments. All experiments held on animals were done according to regulations set by the Institutional Animal Ethics Committee, J.N.M.C.H, A.M.U, Aligarh.

The animals were randomly separated and grouped according to the age and weight into the following three groups of five rats each for evaluation of the systemic toxicity of **1**. The day of administration was designated as day 0. Group I of rats received single dose of DMSO intraperitoneally (ip) which served as a control while Group II and Group III received 2.4 and 4.8 mg/kg body weight of single ip doses of complex **1**, respectively. The toxic effects of **1** on kidney and liver tissues were evaluated after 24 h treatment of rats. At the end of experiments, the rats of each group were dissected. Kidneys and liver tissues were removed for histopathologic and biochemical studies.

Histopathologic examination of tissues. After completion of treatments of **1**, the kidney and liver tissues were carefully taken. They were sliced and fixed in Bouins fluid for 24 h. The

tissues were dehydrated with alcohol of graded concentrations and then cleaned in xylene for 10−15 min. Further, they were treated with xylene plus paraffin wax (1:1) for 15 min, and then complete infiltration was occurred with their treatment with only paraffin wax for further 15 min. They were cast into blocks; sections of tissues were then cut on a microtome to 5 μm by using microtome (Rotary type). They were later attached to slide which was pre–smeared with glycerine and albumin (1:1) and allowed to stick to glass slide by keeping them over hot plate (40−45 °C). These slides were then dipped in xylene for 5 min and then rehydrated in alcohol grades. The prepared slides were subsequently stained in haematoxylin−eosin and examined under light microscope. The photographs of the samples were taken and recorded.

***In vivo* systemic studies.** Reduced glutathione (GSH) was determined using the reported method of of Ellman with a slight modifications.[62] Briefly, tissues were homogenized with ice cold 0.1 M phosphate buffer (pH 7.4) in the ratio of 1:10 (w/v) using homogenizer. The samples were precipitated with 10% trichloroacetic acid and centrifuged at 6000 rpm for 5 minutes. The reaction mixture for each tissue contained supernatant, 0.2 M phosphate buffer (pH 8.4), 0.01 M DTNB (Ellman reagent) and distilled water. The whole mixture was vortexed and then read at 412 nm on a spectrophotometer within 15 minutes. The level of GSH was measured in terms of μmol of GSH/g of tissue using a molar extinction coefficient of 1.36×10^4/M cm^{-1} for GSH.

The extent of LPO in tissue homogenates was determined accorded to the method reported earlier by Ohkawa *et al*.[63] The MDA level was measured at 532 nm. The results were expressed in mmol MDA per g of tissue. The MDA equivalents of the sample were calculated using a molar extinction coefficient of 1.56×10^5/M cm^{-1}. The protein level was determined by the reported method.

Supplementary Information

Supplementary data associated with to this article consists additional details which include tables and figures, ESI−MS spectra, ^{13}C and ^{119}Sn NMR. DNA/RNA interaction studies involving emission spectroscopy, circular dichroism, viscosity measurements and FT−IR are also provided. Crystallographic data is also available from the CCDC with CCDC No. 930737.

Acknowledgements

The authors are thankful to *SAIF*, Panjab University, Chandigarh, for NMR and ESI–Mass facility; *STIC*, Cochin University, Cochin, for providing elemental analysis. The authors are grateful to ACTREC, Mumbai for carrying out the cytotoxic studies. We express our gratitude to DST−PURSE programme and DRS−1 (SAP) from UGC, New Delhi, India for their generous financial support. The author (I. Yousuf) expresses his gratitude to *University Grants Commission* (UGC), New Delhi, for Senior Research Fellowship.

REFERENCES

1. F. Bray, A. Jemal, N. Grey, J. Ferlay and D. Forman, *Lancet Oncol*., 2012, **13***,* 790–801.
2. A. Jemal, F. Bray, M. Melissa, J. Ferlay and D. Forman, *Ca Cancer J. clin*., 2011, **61**, 69–90.
3. A.−M. Florea, D. Büsselberg, *Cancers*, 2011, **3**, 1351−1371.
4. J. M. O' Sullivan, R. A. Huddart, A. R. Norman, J. Nicholls, D. P. Dearnaley and A. Horwich, *Ann. Oncol*., 2003, **14**, 91–96.
5. S. C. Kim, D. W. Kim, Y. H. Shim, J. S. Bang, H. S. Oh, S. W. Kim and M. H. Seo, *J. Control. Release*, 2001, **72**, 191–202.
6. N. Muhammad and Z. Guo, *Curr. Opin. Chem. Biol.*, 2014, **19**, 144–153.
7. I. Romero−Canelón and P. Sadler, *J. Inorg. Chem.*, 2013, **52**, 12276−12291.

8. C. G. Hartinger, S. Zorbas−Seifried, M. A. Jakupec, B. Kynast, H. Zorbas and B. K. Keppler, *J. Inorg. Biochem*., 2006, **100**, 891–904.

9 . F. Lentz, A. Drescher, A. Lindauer, M. Henke, R. A. Hilger, C. G. Hartinger, M. E. Scheulen, C. Dittrich, B. K. Keppler and U. Jaehde, *Anti–Cancer Drugs*, 2009, **20**, 97–103.

10. J. M. Rademaker−Lakhai, D. Van Den Bongard, D. Pluim, J. H. Beijnen and J. H. M. Schellens, *Clin. Cancer Res*. 2004, **10**, 3717–3727.

11. S. Pillozzi, L. Gasparoli, M. Stefanini, M. Ristori, M. D′ Amico, E. Alessio, F. Scaletti, A. Becchetti, A. Arcangeli, L. Messori, *Dalton Trans*., 2014, **43**, 12150–12155.

12. M. Gielen, M. Bouâlam, A. Meriem, B. Mahieu, M. Biesemans and R. Willem, *Heteroatom. Chem*., 1992, **3**, 449–452.

13. S. Tabassum and C. Pettinari, *J. Organomet. Chem*., 2006, **691**, 1761–1766.

14. G. N. Kaluderovic, H. Kommera, E. Hey−Hawkins, R. Paschke and S. Gomez−Ruiz, *Metallomics*, 2010, **2**, 419–428.

15. H. Naïli, F. Hajlaoui, T. Mhiri, T. C. O. Mac Leod, M. N. Kopylovich, K. T. Mahmudov and A. J. L. Pombeiro, *Dalton Trans.*, 2013, **42**, 399–406.

16. N. L. Nkhili, W. Rekik, T. Mhiri, K. T. Mahmudov, M. N. Kopylovich and H. Naïli, *Inorg. Chim. Acta*, 2014, **412**, 27–31.

17. F. Li and R. I. Mahato, *Mol. Pharm.*, 2014, **11**, 2539−2552.

18. C. S. Chow and F. M. Bogdan, *Chem. Rev.*, 1997, **97**, 1489−1513.

19. O. Y. Zolotarskaya, A. F. Wagner, J. M. Beckta, K. Valerie, K. J. Wynne and H. Yang, *Mol. Pharm.*, 2012, **9**, 3403−3408.

20. A. Y. Chen, C. Yu, A. Bodley, L. F. Peng and L. F. Liu, *Cancer Res*., 1993, **53**, 132−137.

21. A. Perez−Rebolledo, J. D. Ayala, G. M. de Lima, N. Marchini, G. Bombieri, C. L. Zani, E. M. Souza−Fagundes and H. Beraldo, *Eur. J. Med. Chem*., 2005, **40**, 467–472.

22. C. Pettinari, F. Marchetti, R. Pettinari, D. Martini, A. Drozdov and S. Troyanov, *Inorg. Chim. Acta*, 2001, **325**, 103–114.

23. H. Aghabozorg, E. Motieiyan, A. R. Salimi, M. Mirzaei, F. Manteghi, A. Shokrollahi, S. Derki, M. Ghadermazi, S. Sheshmani and H. Eshtiagh−Hosseini, *Polyhedron*, 2010, **29**, 1453–1464.

24. B. Yearwood, S. Parkin and D. A. Atwood, *Inorg. Chim. Acta*, 2002, **333**, 124–131.

25. C. N. Banti, A. D. Giannoulis, N. Kourkoumelis, A. M. Owczarzak, M. Poyraz, M. Kubicki, K. Charalabopoulos and S. K. Hadjikakou, *Metallomics*, 2012, **4**, 545–560.

26. M. Chauhan, K. Banerjee and F. Arjmand, *Inorg. Chem*., 2007, **46**, 3072−3082.

27. X.–B. Fu, D.–D. Liu, Y. Lin, W. Hu, Z.–W. Mao and X.–Y. Le, *Dalton Trans*., 2014, **43**, 8721–8737.

28. X. Liang, X. Zou, L. Tan and W. Zhu, *J. Inorg. Biochem.*, 2010, **104**, 1259–1266.

29. F. Cui, Y. Yan, Q. Zhang, J. Du, X. Yao, G. Qu and Y. Lu, *Carbohyd. Res.*, 2009, **344**, 642–647.

30. B. K. Paul and N. Guchhait, *J. Phys. Chem*. *B*, 2011, **115**, 11938–11949.

31. S. Mahadevan and M. Palaniandavar, *Inorg. Chem*., 1998, **37**, 693−700.

32. (a) M. Vorlickova, *Biophys. J*., 1995, **69**, 2033−2043; (b) J. Kypr and M. Vorlickova, *Biopolymers* (*Biospectroscopy*), 2002, **67**, 275−277.

33. E. Froehlich, E. J. S. Mandeville, D. Arnold, L. Kreplak and H. A. Tajmir−Riah, *Biomacromolecules*, 2012, **13**, 282−287.

34. S. Satyanarayana, J. C. Dabrowiak and J. B. Chaires, *Biochemistry*, 1993, **32**, 2573−2584.

35. H. Xu, Y. Liang, P. Zhang, F. Du, B.–R. Zhou, J. Wu, J.–H. Liu, Z.–G. Liu and L.–N. Ji, *J. Biol. Inorg. Chem.*, 2005, **10**, 529–538.

36. C. N. N′ soukpoe−Kossi, A. A. Ouameur, T. Thomas, A. Shirahata, T. J. Thomas and H. A. Tajmir−Riahi, *Biomacromolecules*, 2008, **9**, 2712–2718.

37. F. Arjmand and M. Muddassir, *J. Photochem. Photobiol. B: Biol*., 2010, **101**, 37–46.

38. H. Arakawa, J. F. Neault and H. A. Tajmir−Riahi, *Biophy. J*., 2001, **81**, 1580–1587.

39. J. F. Neault and H. A. Tajmir−Riahi, *J. Phys. Chem. B*, 1997, **101**, 114–116.

40. A. Casini, L. Messori, P. Orioli, M. Gielen, M. Kemmer and R. Willem, *J. Inorg. Biochem*., 2001, **85**, 297–300.

41. F. Arjmand, F. Sayeed, S. Parveen, S. Tabassum, A. S. Juvekar and S. M. Zingde, *Dalton Trans.*, 2013, **42**, 3390− 3401.

42. P. Katkar, A. Coletta, S. Castelli, G. L. Sabino, R. A. A. Couto, A. M. C. Ferreira and A. Desideri, *Metallomics*, 2014, **6**, 117−125.

43. (a) Y. Pommier, E. Leo, H. L. Zhang and C. Marchand, *Chem. Biol.* 2010, **17**, 421−433; (b) R. A. Khan, A. Asim, R. Kakkar, D. Gupta, V. Bagchi, F. Arjmand, and S. Tabassum, *Organometallics*, 2013, **32**, 2546−255

44. T. X. Nguyen, A. Morrell, M. Conda−Sheridan, C. Marchand, K. Agama, A. Bermingam, A. G. Stephen, A. Chergui, A. Naumova, R. Fisher, B. R. O′ Keefe, Y Pommier and M. Cushman, *J. Med. Chem*., 2012, **55**, 4457−4478.

45. S. Neidle, *Nat. Prod. Rep.*, 2001, **18**, 291–309.

46. Y. Gilad and H. Senderowitz, *J. Chem. Inf. Model*., 2014, **54**, 96−107.

47. D. Agudelo, P. Bourassa, M. Beauregard, G. Berube and H.–A. Tajmir−Riahi, *Plosone*, 2013, **8**, e69248.

48. H. T. M. Van and W.−J. Cho, *Bioorg. Med. Chem. Lett.* 2009, **19**, 2551–2554.

49. S. Tabassum, W. M. Al−Asbahy, M. Afzal, F. Arjmand and V. Bagchi, *Dalton Trans*., 2012, **41**, 4955–4964.

50. T. Lammers, P. Peschke, V. Ehemann, J. Debus, B. Slobodin, S. Lavi and P. Huber, *Mol. Cancer*, 2007, **6**, 65–78.

51. Y. Zaidi, F. Arjmand, N. Zaidi, J. A. Usmani, H. Zubair, K. Akhtar, M. Hossain and G. G. H. A. Shadab, *Metallomics*, 2014, **6**, 1469−1479.

52. J. Marmur, *J. Mol. Biol*., 1961, **3**, 208−218.

53. K. A. Meadows, F. Liu, J. Sou, B. P. Hudson and D. R. McMillin, *Inorg. Chem*., 1993, **32**, 2919−2923.

54. A. Altomare, M. C. Burla, M. Camalli, G. L. Cascarano, C. Giocavazzo, A. Guagliardi, A. G. C. Moliterni, G. Polidori and S. Spagna, *J. Appl. Crystallogr.*, 1999, **32**, 115–119.

55. G. M. Sheldrick, SHELX–97, *Program for Crystal Structure refinement, University of Göttingen*, Germany, 1997.

56. A. L. Spek, PLATON Procedure, *A multipurpose Crystallographic Tool, Utrecht University*, Utrecht, The Netherlands, 1998.

57. J. R. Lakowicz and G. Webber, *Biochemistry*, 1973, **12**, 4161–4170.

58. A. Wolfe, G. H. Shimer Jr. and T. Meehan, *Biochemistry*, 1987, **26**, 6392–6396.

59. F. Arjmand, M. Muddassir, Y. Zaidi and D. Ray, *Med. Chem. Commun*., 2011, **14**, 394–405.

60. F. Arjmand, I. Yousuf, M. Afzal and L. Toupet, *Inorg. Chim. Acta*, 2014, **421**, 26–37.

61. (a) D. Mustard and D. W. Ritchie, *Proteins: Struct. Funct. Bioinf.*, 2005, **60**, 269–274; (b) G. Macindoe, L. Mavridis, V. Venkatraman, M.–D. Devignes and D. W. Ritchie, *Nucl. Acids Res.*, 2010, **38**, 445–449.

62. G. L. Ellman, *Arch. Biochem. Biophys.*, 1959, **82**, 214−226.

63. H. Ohkawa, N. Ohishi and K. Yagi, *Anal. Biochem*., 1979, **95**, 351−358.

Tables and Figures

Table 1. The binding constant (K_b) values of complex **1** with the ct–DNA and yeast t–RNA (mean standard deviation).

Nucleic acids	λ_{max} (nm)	K_b (M^{-1})	% hyperchromism
ct–DNA	270	5.12(±0.15) x 10^4	37%
yeast tRNA	270	7.56(±0.09) x 10^4	43%

Table 2. Summary of the screening data for the *in vitro* cytotoxic activity of complex **1** (in µg/ml)

Cell line		U373MG	PC3	Hop62	HL60	HCT15	SK–OV–3	HeLa	MCF7
GI_{50}	**Complex 1**	49.0	<10	<10	<10	<10	<10	<10	<10
	ADR	53.0	<10	<10	<10	<10	<10	<10	<10
TGI	**Complex 1**	>80	16.7	<10	25.5	18.2	<10	17.7	14.2
	ADR	>80	12.7	21.9	31.9	40.0	44.4	12.8	22.6
LC_{50}	**Complex 1**	>80	59.3	33.3	68.7	53.0	35.5	53.4	54.2
	ADR	>80	52.8	53.3	75.5	>80	>80	53.4	56.4

GI_{50} = growth inhibition of 50% (GI_{50}) calculated from [(Ti−Tz)/(C−Tz)] x 100 = 50, drug concentration that results in a 50% reduction in the net protein increase.
ADR = Adriamycin (taken as positive control compound).
GI_{50}value < 10 µM is considered to demonstrate activity.
TGI = tumor growth inhibition.
LC_{50}= lethal concentration of 50% (LC_{50}).

Table 3. Effect of **1** on levels of reduced glutathione (GSH) and lipid peroxidation (expressed as malondialdehyde; MDA) in kidney tissue of female Wistar rats sacrificed 24 h after the ip administration.

Groups Dose: mg/kg	**µmol GSH/g of tissue**	**% of control**	**µmol MDA/g of tissue**	**% of control**
Control	2.19 ± 0.31^{a}	100	0.12 ± 0.04^{a}	100
Complex 1				
2.4	1.88 ± 0.08^{a}	85	0.16 ± 0.02^{a}	133
4.8	1.49 ± 0.08^{b}	68	0.21 ± 0.02^{b}	175

Values that show different lowercase letters (a,b) differ significantly at $p = 0.05$ (one–way ANOVA followed by Tukey test).

Table 4. Effect of **1** on levels of reduced glutathione (GSH) and lipid peroxidation (expressed as malondialdehyde; MDA) in Liver tissue of female Wistar rats sacrificed 24 h after the ip administration**.**

Groups Dose: mg/kg	**µmol GSH/g of tissue**	**% of control**	**µmol MDA/g of tissue**	**% of control**
Control	1.96 ± 0.11^{a}	100	0.13 ± 0.03^{a}	100
Complex 1				
2.4	1.84 ± 0.05^{a}	94	0.17 ± 0.02^{a}	130
4.8	1.79 ± 0.05^{b}	91	0.22 ± 0.03^{b}	169

Values that show different lowercase letters (a,b) differ significantly at $p = 0.05$ (one–way ANOVA followed by Tukey test).

Table 5. Selected crystallographic data for the complex **1**.

Parameters	
Empirical formula	$C_8H_{17}Cl_4N_3O_4Sn$
Formula weight (g mol^{-1})	479.74
Crystal system	Monoclinic
Space group	*Ima2*
a (Å)	13.9718(3)
b (Å)	9.8400(2)
c (Å)	11.9523(3)
α (deg)	90
β(deg)	90
γ (deg)	90
U ($Å^3$)	1643.23(6)
Z	4
ρ_{calc} (g/cm^3)	1.939
μ (mm^{-1})	2.218
F(000)	944.0
crystal size (mm)	0.24 × 0.20 × 0.11
Temp (K)	150(2)
measured reflns	6402
unique reflns	1782
θ Range (deg)/completeness (%)	2.92 to 27.00/0.998
GOF[a]	1.000
R[b][I>2σ(I)]	0.0188
wR_2[b] (all data)	0.0388
largest diff. peak/hole (e.$Å^{-3}$)	0.265/ −0.303

[a]GoF is defined as $\{\Sigma[w(F_0^2-F_c^2)]/(n-P)\}^{1/2}$ where n is the number of data and p is the number of parameters. [b]$R = \{\Sigma||F_0|-|F_c||/\Sigma|F_0|$, $wR^2 = \{\Sigma\, w(F_0^2-F_c^2)^2 / \Sigma\, w(F_0^2)^2\}^{1/2}$

Figure Captions

Fig. 1. Schematic representation of the specific recognition domains in ionic tin(IV) iminodiacetic acid–piperazinediium conjugate (**1**).

Fig. 2. (a) Molecular structure of **1** along with atom numbering scheme drawn with 50% probability ellipsoids. (b) Intermolecular hydrogen bonded 1D polymeric array along *a* axis in complex **1**. (Hydrogen atoms are omitted for clarity)

Fig. 3. Absorption spectral traces of complex **1** in 5mM Tris HCl/50 mM NaCl buffer at pH 7.2 upon addition of (a) ct–DNA and (b) yeast tRNA at 25 °C. Inset: Plots of [DNA or RNA]/ε_a–ε_f (M^2cm) *vs* [DNA or RNA] for the titration with **1**, ■ experimental data points, full lines, linear fitting of the data. [DNA], [RNA] = 0.0–6.0 x 10^{-5} M, [Complex **1**] = 1.66 x 10^{-4} M.

Fig. 4. Agarose gel electrophoresis patterns for the cleavage of pBR322 plasmid (300 ng) as a function of increasing concentration of **1** at 310 K after 45 min of incubation at different concentrations; Lane 1: DNA control; Lane 2: 10 μM of **1**+DNA**;** Lane 3: 20 μM of **1**+DNA; Lane 4: 30 μM of **1**+DNA; Lane 5: 40 μM of **1**+DNA; Lane 6: 50 μM of **1**+DNA.

Fig. 5. Agarose gel electrophoresis showing effect of different concentration of complex **1** on the activity of DNA topoisomerase I (Topo I); Lane 1, DNA control; Lane 2, Topo I + DNA; Lane 3, 15 μM of **1** + DNA + Topo I; Lane 4, 20μM of **1** + DNA + Topo I; Lane 5, 25 μM of **1**+ DNA + Topo I; Lane 6, 30 μM of **1** + DNA + Topo I.

Fig. 6. Molecular docked model of **1** fitted into G–C region of the minor groove of DNA dodecamer duplex of sequence d$(CGCGAATTCGCG)_2$ along with its possible hydrogen bonding interactions .

Fig. 7. Full−length structure of yeast $tRNA^{Phe}$ (PDB code 6TNA). (a) The base sequence is drawn in the cloverleaf form. (b) A 3−Dimensional ribbon diagram of tRNA; The Acceptor stem is colored orange, the D arm is cyan, the Anticodon arm is deep green, the TψC arm is yellow, the Variable loop is light green and the CCA terminus is red. The green colored balls represents Mg^{2+} ions.

Fig. 8. Molecular docked model of complex **1** docked into the active pocket of anticodon arm of yeast tRNA (PDB ID: 6TNA).

Fig. 9. Molecular docked model of **1** with the human–DNA–Topo−I (PDB ID: 1SC7). (a) Occupying chemically significant site, adjacent to G–C base pairs of the minor groove of the DNA. (b) H−bonding interactions of complex **1** with amino acid residues at the binding site of Topo I.

Fig. 10. Growth curve showing % control growth *vs* drug concentration (μg ml^{-1}) against different human carcinoma cell lines: U373MG (CNS), PC3 (Prostate), Hop62 (Lung), HCT15 (Colon), SK−OV−3 (Ovarian), HeLa (Cervix) and MCF7 (Breast), HL60 (Leukaemia).

Fig. 11. Light micrographs of kidneys and livers from female Wistar rats injected with control (A, D); 2.4 mg kg^{-1} dosage of **1** (B, E); 4.8 mg kg^{-1} dosage of **1** (C, F) (hematoxylin and eosin stain).Original magnifications:x400. The features characterize manifestations of **1** nephrotoxicity and hepatotoxicity at concentration of 2.4 and 4.8 mg kg^{-1}: DT, distal tubule; G, glomeruli; PT, proximal tubule; Inf, inflammation; CPV, congested portal vein; Hc, hepatocyte; CV, cental vein.

Figures and Schemes

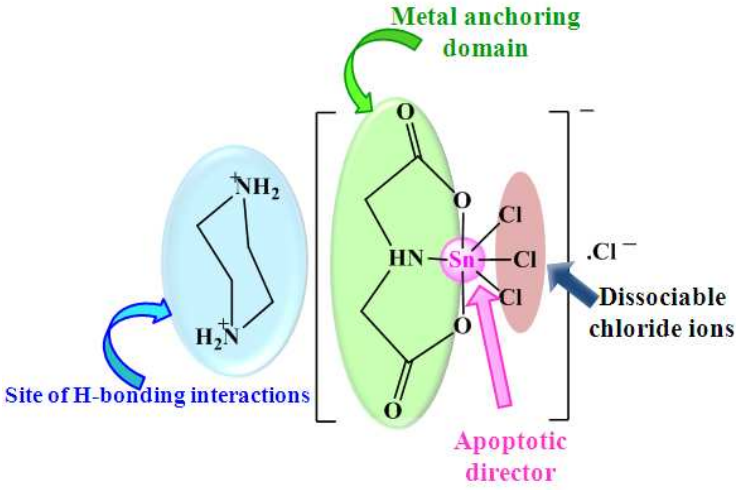

Fig. 1

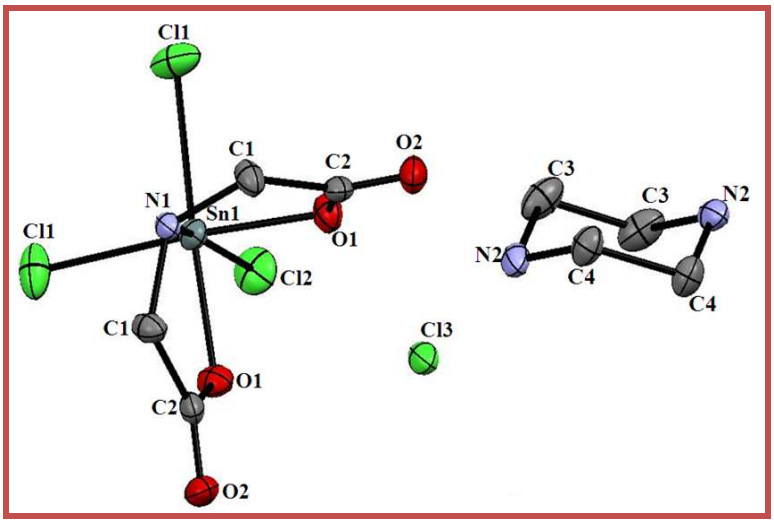

Fig. 2a

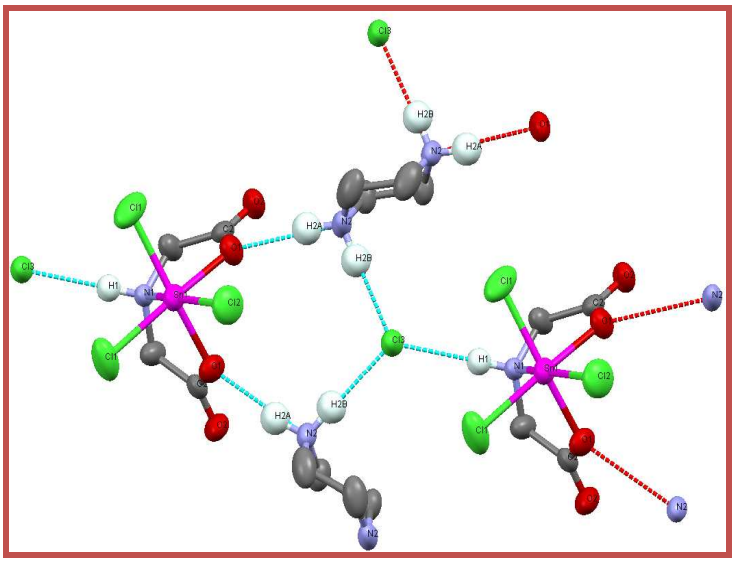

Fig. 2b

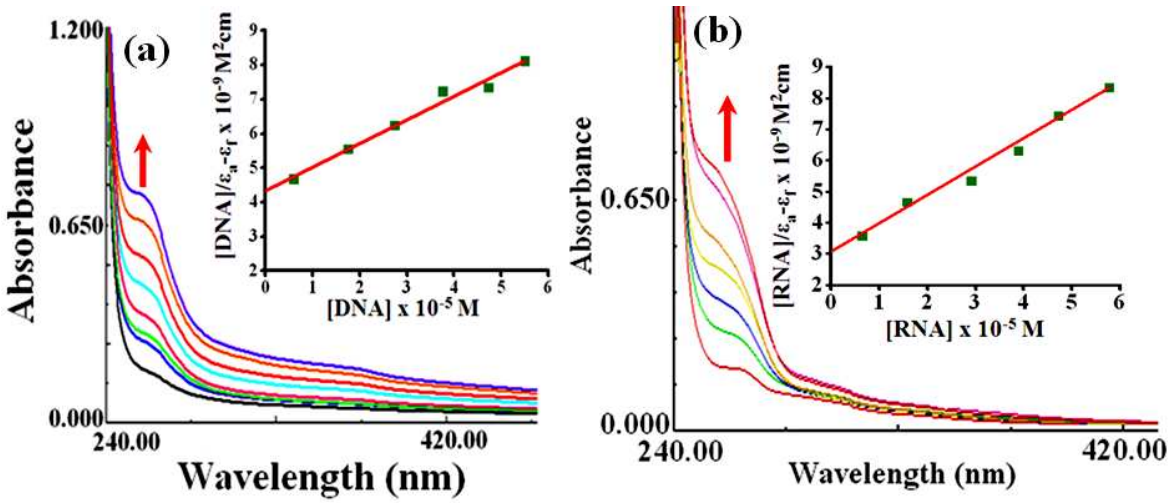

Fig. 3

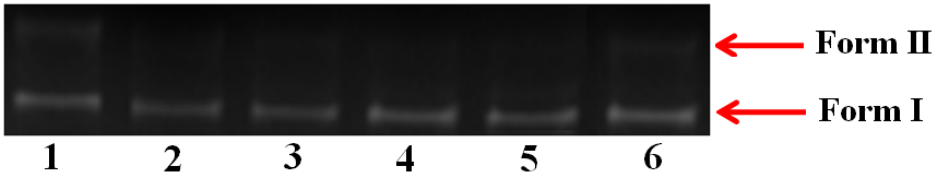

Fig. 4

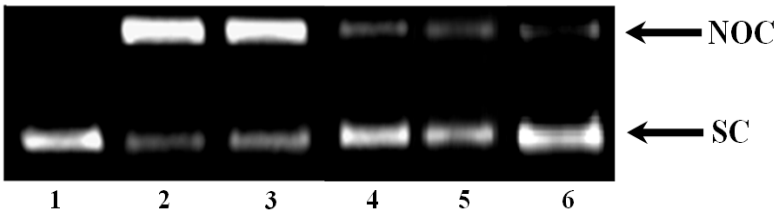
NOC
SC
1
2
3
4
5
6

Fig. 5

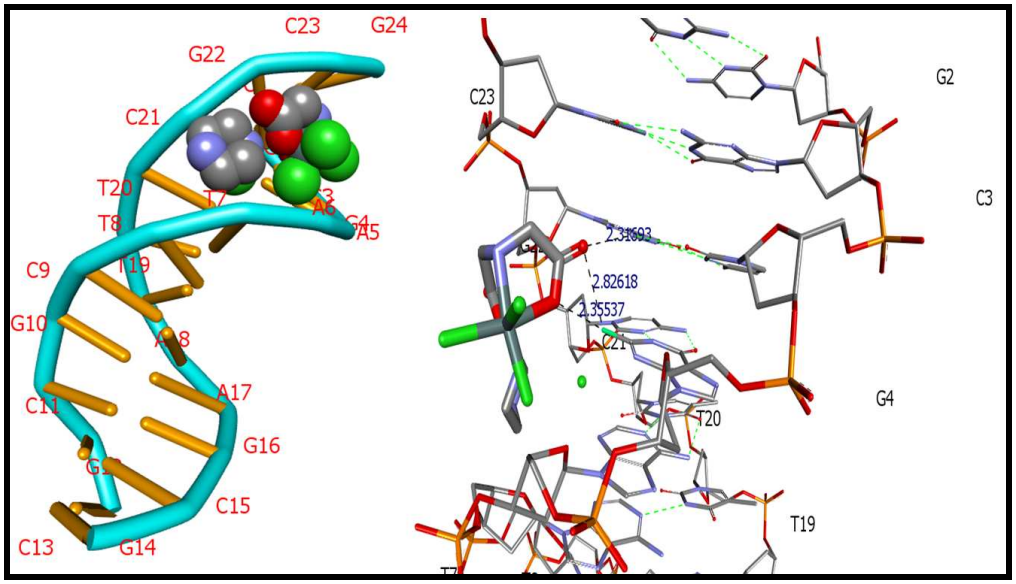
C23
G24
G22
C21
T20
T8
C9
G10
C11
A17
G16
C15
C13
G14
A5
C23
G2
C3
2.82618
2.35537
G4
T20
T19

Fig. 6

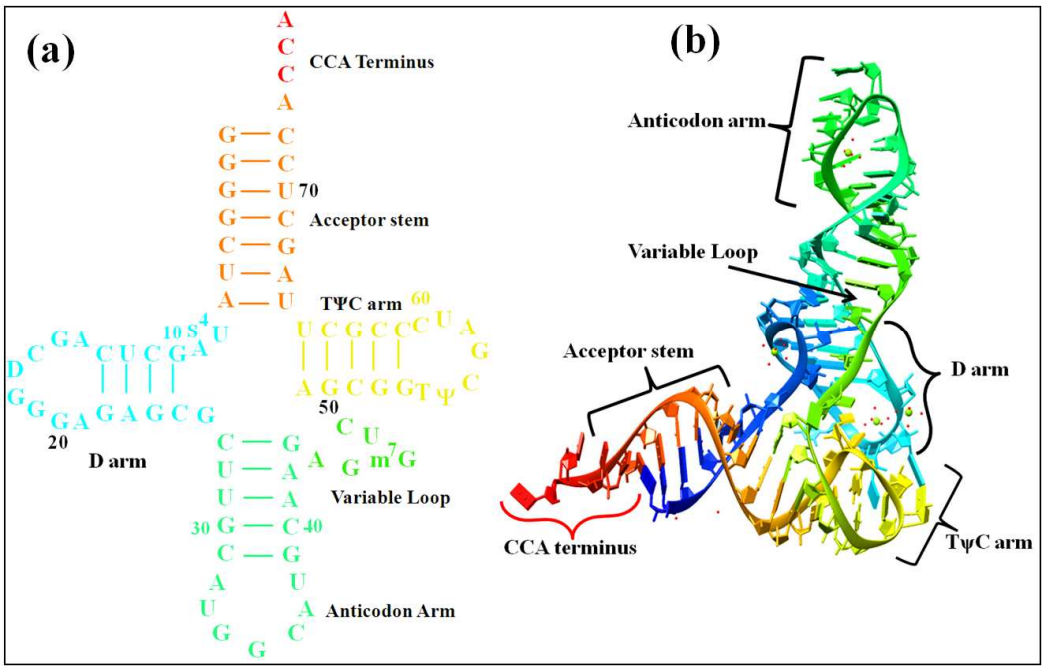
(a)
CCA Terminus
Acceptor stem
TΨC arm
Variable Loop
D arm
Anticodon Arm
(b)
Anticodon arm
Variable Loop
Acceptor stem
D arm
CCA terminus
TψC arm

Fig. 7

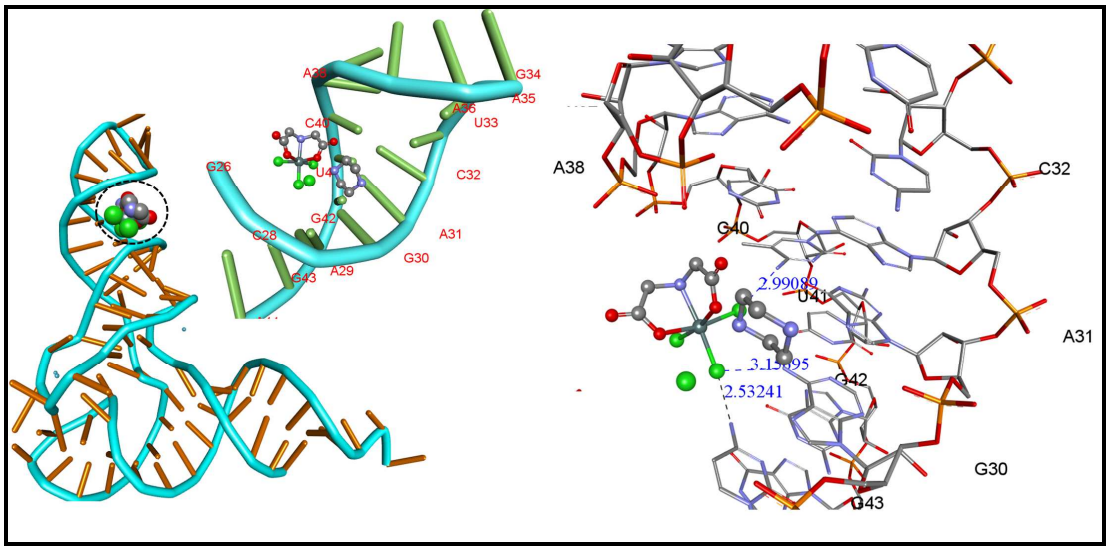
A38
C32
G40
U41
A31
G42
G30
G43
2.99089
2.53241

Fig. 8

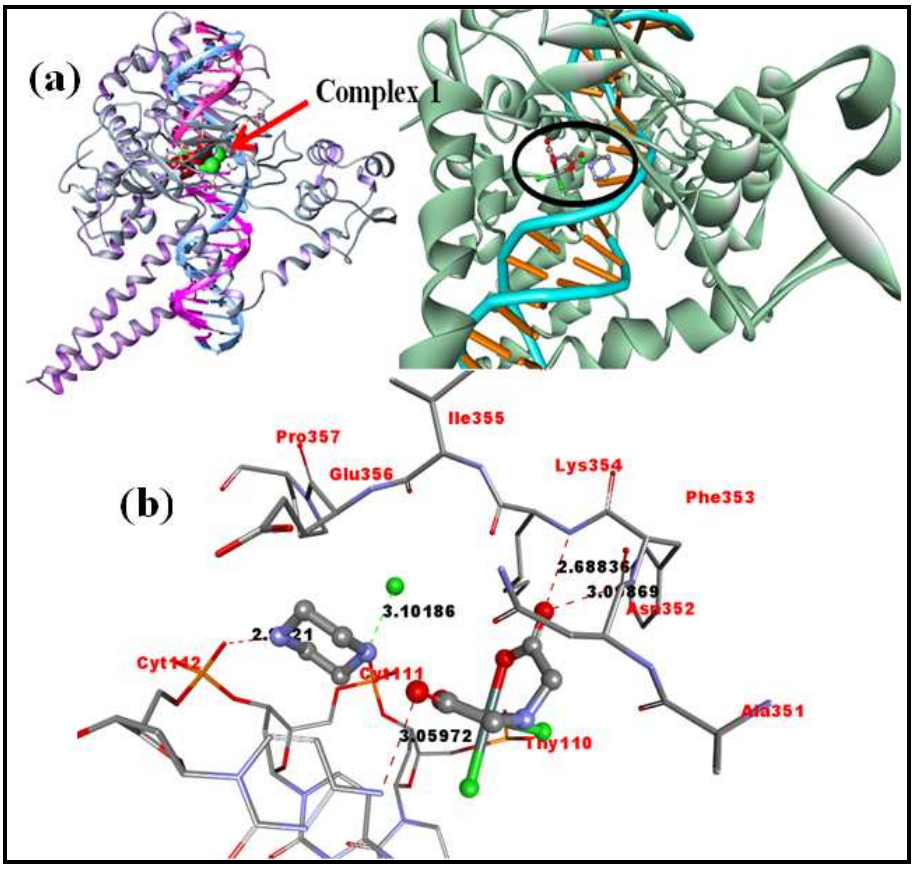
(a)
Complex 1
(b)
Ile355
Pro357
Glu356
Lys354
Phe353
2.68836
3.10186
Asp352
Cyt142
Cyt111
Ala351
3.05972
Thy110

Fig. 9

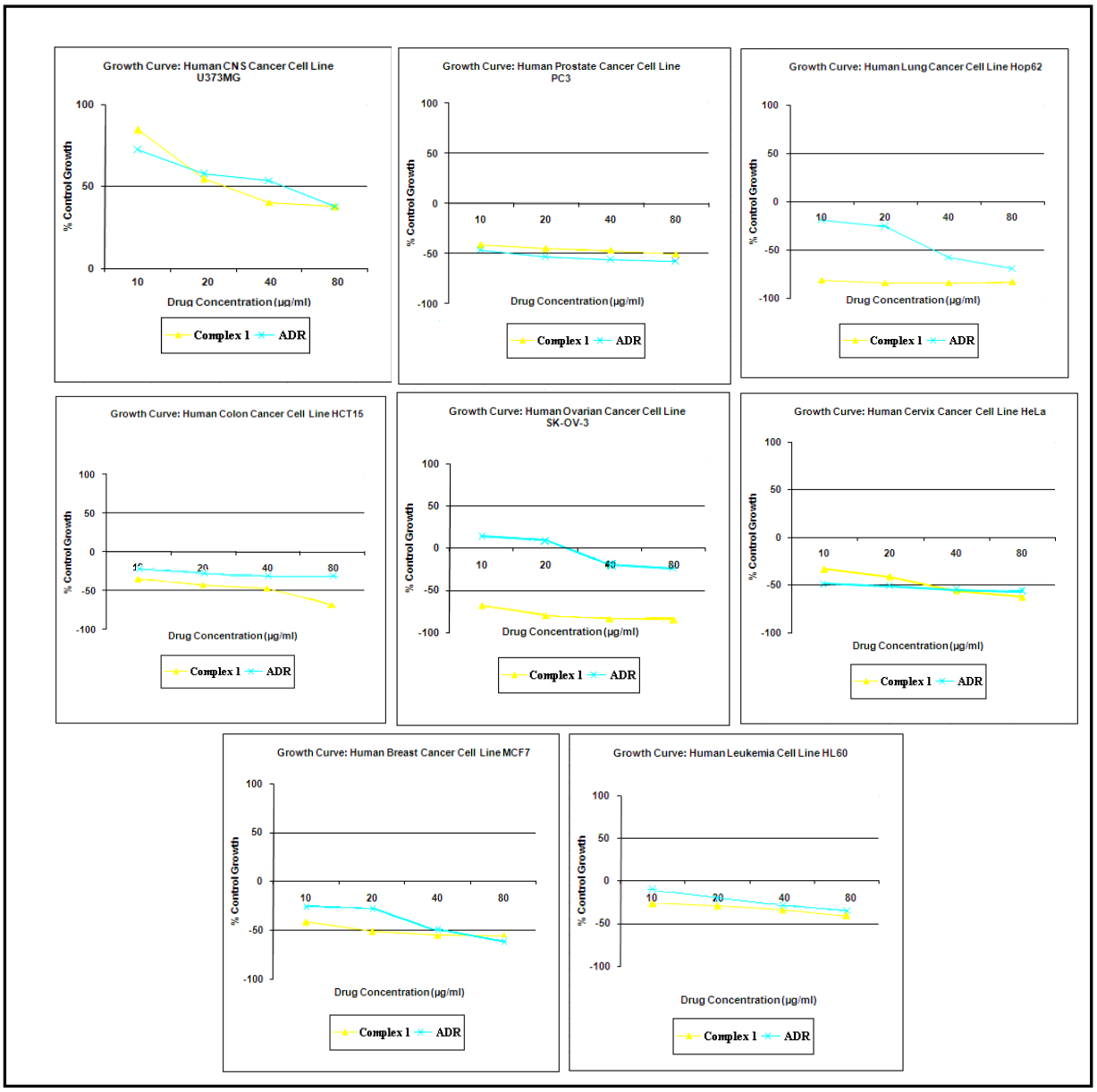
Growth Curve: Human CNS Cancer Cell Line U373MG
Growth Curve: Human Prostate Cancer Cell Line PC3
Growth Curve: Human Lung Cancer Cell Line Hop62
Growth Curve: Human Colon Cancer Cell Line HCT15
Growth Curve: Human Ovarian Cancer Cell Line SK-OV-3
Growth Curve: Human Cervix Cancer Cell Line HeLa
Growth Curve: Human Breast Cancer Cell Line MCF7
Growth Curve: Human Leukemia Cell Line HL60
% Control Growth
Drug Concentration (µg/ml)
Complex 1
ADR

Fig. 10

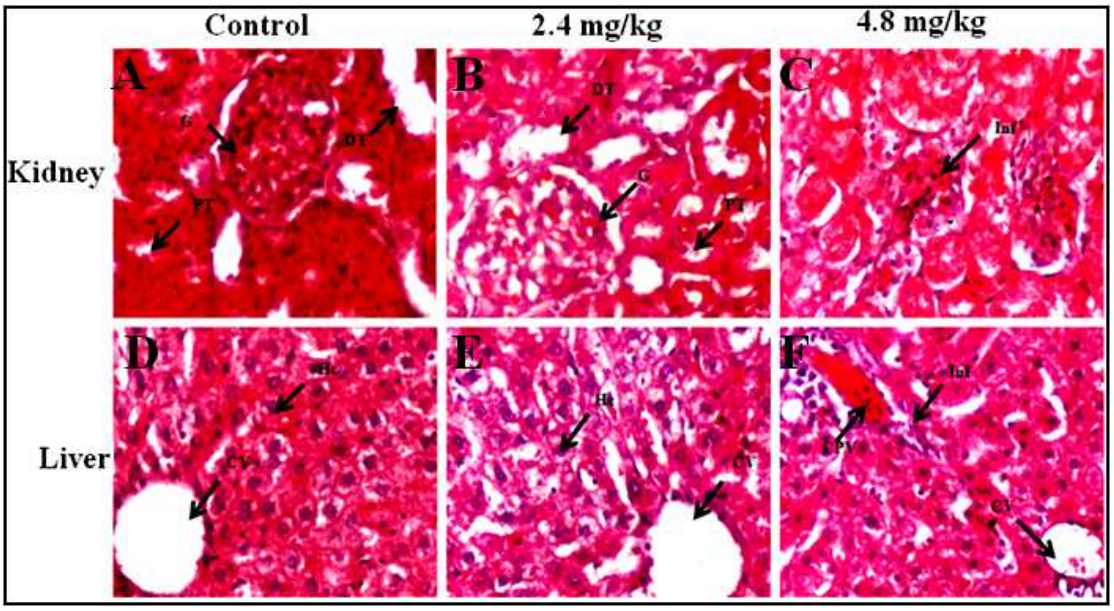

Fig. 11

Scheme 1. Synthetic route for complex **1.**

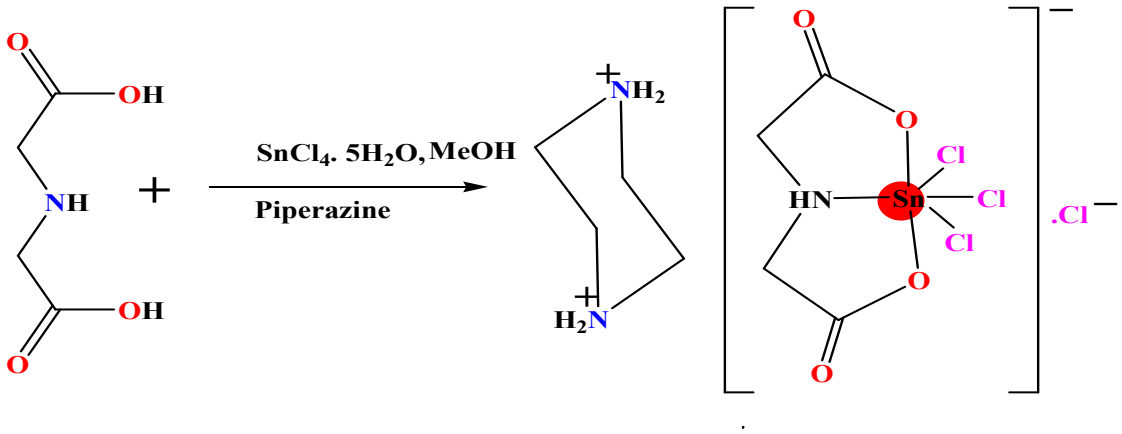

Scheme 2. Mechanistic details of topoisomerase I inhibition activity by complex.